PHYSICS

Ubiquitous defect-induced density wave instability in monolayer graphene

A. C. Qu[1,2], P. Nigge[1,2], S. Link[3], G. Levy[1,2], M. Michiardi[1,2,4], P. L. Spandar[5], T. Matthé[1,2], M. Schneider[1,2], S. Zhdanovich[1,2], U. Starke[3], C. Gutiérrez[1,2,5]*, A. Damascelli[1,2]*

Quantum materials are notoriously sensitive to their environments, where small perturbations can tip a system toward one of several competing ground states. Graphene hosts a rich assortment of such competing phases, including a bond density wave instability ("Kekulé distortion") that couples electrons at the K/K′ valleys and breaks the lattice symmetry. Here, we report observations of a ubiquitous Kekulé distortion across multiple graphene systems. We show that extremely dilute concentrations of surface atoms (less than three adsorbed atoms every 1000 graphene unit cells) can self-assemble and trigger the onset of a global Kekulé density wave phase. Combining complementary momentum-sensitive angle-resolved photoemission spectroscopy (ARPES) and low-energy electron diffraction (LEED) measurements, we confirm the presence of this density wave phase and observe the opening of an energy gap. Our results reveal an unexpected sensitivity of the graphene lattice to dilute surface disorder and show that adsorbed atoms offer an attractive route toward designing novel phases in two-dimensional materials.

INTRODUCTION

A density wave (DW) is a phase of matter that features a spatially modulated quantity (charge, spin, or bond order) and, in many cases, is accompanied by a periodic distortion of the crystal lattice (*1*). These spatial modulations break the translational symmetry of the host crystal, resulting in a reconstruction of the Fermi surface that can open energy gaps in the electronic spectrum. DW phases have been found in a myriad of systems and can coexist or compete with other correlated phases, such as superconducting and Mott insulating states (*2*–*4*). In one-dimensional systems, DW formation—also called the Peierls transition—is thought to be driven primarily by a divergent electronic response to charge modulations with wave vector $\delta\boldsymbol{q} = 2k_F$ that connects (or nests) the two points of the Fermi surface (*1*, *5*). However, the mechanism for DW formation in higher-dimensional systems, where Fermi surface nesting is imperfect, is still highly debated (*6*–*8*).

Graphene, the prototypical two-dimensional material, presents an ideal tunable system for exploring DW formation: (i) At zero doping, its Fermi "surface" consists of two perfectly nested points (K/K′) at its Brillouin zone (BZ) corners connected by wave vector $\delta\boldsymbol{q} = \boldsymbol{K} - \boldsymbol{K}'$; (ii) it features strong electron-phonon coupling and soft K-point phonon and plasmon modes (*9*–*12*); and (iii) its charge density, and thus the size of the Fermi surface and the DW nesting condition, can be tuned with electrostatic gating or substrate charge transfer. Owing to these unique properties, and the fourfold degeneracy of its spin and valley degrees of freedom, graphene has been shown to host a plethora of ordered electronic phases. One such phase is the Kekulé distortion (*13*–*17*), a bond DW phase that has been described as a Peierls-like (*5*) lattice instability intrinsic to systems with relativistic dispersions (*13*, *18*, *19*). Undistorted graphene is composed of a honeycomb lattice of carbon atoms that exhibits sixfold bond symmetry (Fig. 1A). Its low-energy band structure is described by two inequivalent and gapless Dirac cones at K/K′ (Fig. 1B). In the Kekulé phase, the bond symmetry breaks such that the unit cell is tripled in size (thin/thick bonds; Fig. 1C). The new commensurate $(\sqrt{3} \times \sqrt{3})R30°$ bonding pattern can be centered at one of three equivalent carbon hollow sites—distinguished by the use of red-gray-blue (RGB) color tiling in Fig. 1C—and reflects the particular phase of the Kekulé order parameter. This supercell causes the previously inequivalent Dirac cones at K/K′ to be connected by a reciprocal lattice vector, which leads to a Fermi surface reconstruction that folds each cone to the Kekulé BZ center at Γ (Fig. 1D). Different topological Kekulé phases are determined by the specific broken C—C bond symmetry: The "O"-shaped pattern (Fig. 1C) opens an energy gap of $2\Delta_K$ at the Dirac point (*13*, *14*, *20*) (Fig. 1D), while other "Y"-shaped patterns are gapless (*21*–*24*) (see the Supplementary Materials). When additionally allowing for a possible A-B sublattice symmetry breaking term, Δ_{AB}, the total low-energy Kekulé dispersion is given by (*25*) (see Materials and Methods)

$$\varepsilon(k) = \pm\sqrt{\hbar^2 v_F^2 k^2 + \Delta_{AB}^2 + |\Delta_K|^2} \quad (1)$$

where $\hbar$ is Planck's constant divided by 2π, v_F is the Fermi velocity, and k is the crystal momentum.

To date, there have been few direct experimental observations of the graphene Kekulé phase (*20*, *23*, *26*–*28*). In theory, it can arise through several mechanisms: electron-electron (*12*, *14*, *17*) and electron-phonon interactions (*13*, *29*) at high magnetic fields (*15*, *26*, *28*, *30*); from high-density $(\sqrt{3} \times \sqrt{3})R30°$ adatom superlattices (*22*, *27*, *31*–*33*); and large biaxial strain (*34*, *35*). The nature of the Kekulé phase is of fundamental interest as it provides an example of spontaneous gap formation via K/K′ valley ("chiral") symmetry breaking (*15*, *16*, *25*, *36*), and it has been predicted to host topological defects with fractionalized charge (*14*). Most recently, the Kekulé phase and coupled intervalley states have attracted attention as candidates for the correlated insulating states in twisted bilayer graphene (*37*–*41*). Here, we report a controllable method for inducing the Kekulé DW phase in graphene through the self-assembly of

[1]Department of Physics and Astronomy, University of British Columbia, Vancouver, Canada. [2]Quantum Matter Institute, University of British Columbia, Vancouver, Canada. [3]Max Planck Institute for Solid State Research, Stuttgart, Germany. [4]Max Planck Institute for the Physics of Complex Systems, Dresden, Germany. [5]Department of Physics and Astronomy, University of California, Los Angeles, Los Angeles, CA, USA.
*Corresponding author. Email: gutierrez@physics.ucla.edu (C.G.); damascelli@physics.ubc.ca (A.D.)

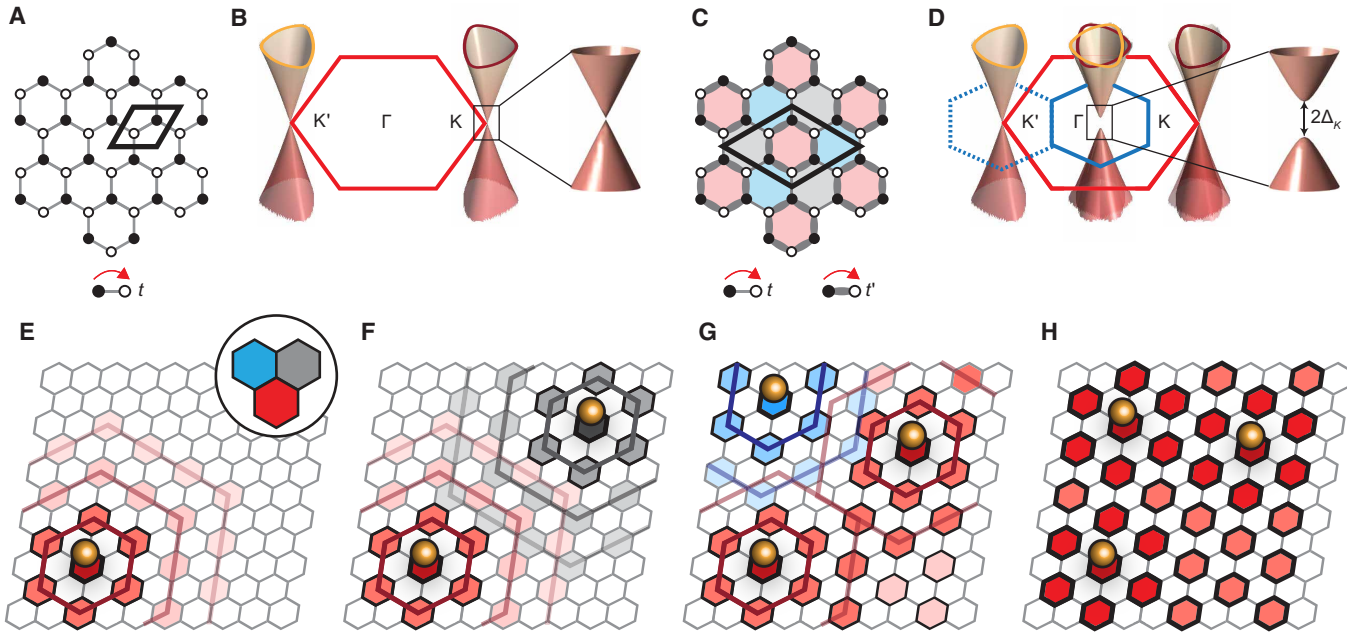

Fig. 1. The Kekulé phase and hidden Kekulé ordering of lithium on graphene. (**A**) Schematic diagram of pristine graphene. The diamond indicates the primitive unit cell. All bonds between adjacent atoms are equivalent owing to the same hopping energy, *t*. (**B**) Schematic diagram of the graphene band structure composed of two gapless Dirac cones K/K′ located at the corners of the BZ (red hexagon). (**C**) Schematic diagram of Kekulé distorted graphene. The bond symmetry breaks (thin, thick lines) owing to new hopping energies (*t*/*t*′), forming a $(\sqrt{3} \times \sqrt{3})R30°$ superstructure and tripling the size of the unit cell (diamond). The tripled supercell can be visualized by the red-gray-blue (RGB) coloring of the three inequivalent hexagonal plaquettes. (**D**) The superstructure leads to a smaller BZ (blue hexagon) and the K/K′ Dirac cones being folded to Γ, as well as a gap opening at the Dirac point. At energies above the Dirac point, the folded trigonal bands intersect, producing a Star of David pattern. The intensity of folded bands at K/K′ is exaggerated for clarity. (**E**) A single adatom on graphene produces Friedel oscillations with a local $(\sqrt{3} \times \sqrt{3})R30°$ structure on a red site, one of three equivalent colored sites (inset). Bond distortions (thick lines) appear near the adatom. (**F** to **H**) Additional adatoms produce their own Friedel oscillations on out-of-phase sites (blue, gray). The mobile adatoms interact through their Friedel oscillations, preferring to occupy red sites where the oscillations interfere constructively. Hidden Kekulé order occurs when a majority of adatoms occupy one of the RGB sites, inducing the Kekulé distortion globally.

an extremely dilute concentration of lithium adatoms (<0.3% surface coverage or less than three adsorbed atoms every 1000 graphene unit cells). Using angle-resolved photoemission spectroscopy (ARPES) (*42*), we probe the electronic band structure of this DW phase and directly image the folded Dirac cones at the BZ center, as well as observe the opening of an energy gap of $2\Delta_K \approx 200$ meV at the Dirac point, the two signatures of the Kekulé-O phase in graphene.

We induce the Kekulé-O phase (henceforth simply referred to as Kekulé) in graphene through electron-mediated self-assembly of lithium (Li) adatoms. Atomically sharp defects such as adatoms on graphene can scatter electrons between valleys K and K′, producing unique long-range Friedel oscillations with a hexagonal $(\sqrt{3} \times \sqrt{3})R30°$ pattern and period determined by scattering wave vectors that satisfy the Kekulé nesting condition $\delta\boldsymbol{q} = \boldsymbol{K} - \boldsymbol{K}'$ (*43*–*49*). Each Li adatom site thus nucleates a local patch of Kekulé DW order of radius ~2 to 5 nm (*47*), resulting in symmetry breaking between the three previously equivalent RGB Kekulé "colors" (Fig. 1, E and F). Other mobile Li adatoms interact with the long-range $(\sqrt{3} \times \sqrt{3})R30°$ charge modulations, preferring an arrangement that allows their Friedel oscillations to be in phase (Fig. 1G). The constructive interference between several adatom-induced oscillations on a single-"color" site produces enhanced charge-density modulations and, through electron-phonon coupling, the emergence of the Kekulé distortion throughout graphene—even when the adatoms themselves may be many unit cells apart (Fig. 1H) (*45*, *46*). The adatoms are said to observe hidden Kekulé order, since without the RGB color scheme, the long-range adatom ordering would be obscured (*45*, *46*).

RESULTS

In Fig. 2A, we show ARPES data from pristine monolayer epitaxial graphene on silicon carbide (Gr/SiC) (*50*). ARPES energy-momentum maps are plotted along the yellow cut in momentum space shown in Fig. 2C, at the graphene K point. Because of charge transfer from the substrate, the Dirac point is shifted to ≈430 meV below the Fermi level E_F (*50*–*52*). The observed intensity asymmetry of the two branches of the Dirac cone in Fig. 2A is due to the experimental geometry and the polarization of the ultraviolet light source (*53*). Momentum distribution curves (MDCs) at each binding energy are fit with two Lorentzians, whose peak positions are indicative of the electronic dispersions of the conduction and valence bands (thick yellow lines, Fig. 2A). Close to the Fermi energy, the dispersions are well described by linear fits (thin yellow lines, Fig. 2A) above and below the Dirac point at −430-meV binding energy. For massless Dirac fermions, the extrapolated fits from the two energy bands would cross at the Dirac point. Such crossing, however, is not observed. The origin of this apparent energy gap has been attributed to a sublattice symmetry breaking term (Δ_{AB} in Eq. 1) (*51*, *54*) or band renormalization due to electron-plasmon effects (*52*, *55*). As we describe below, the precise microscopic origin of the preexisting gap in pristine Gr/SiC is

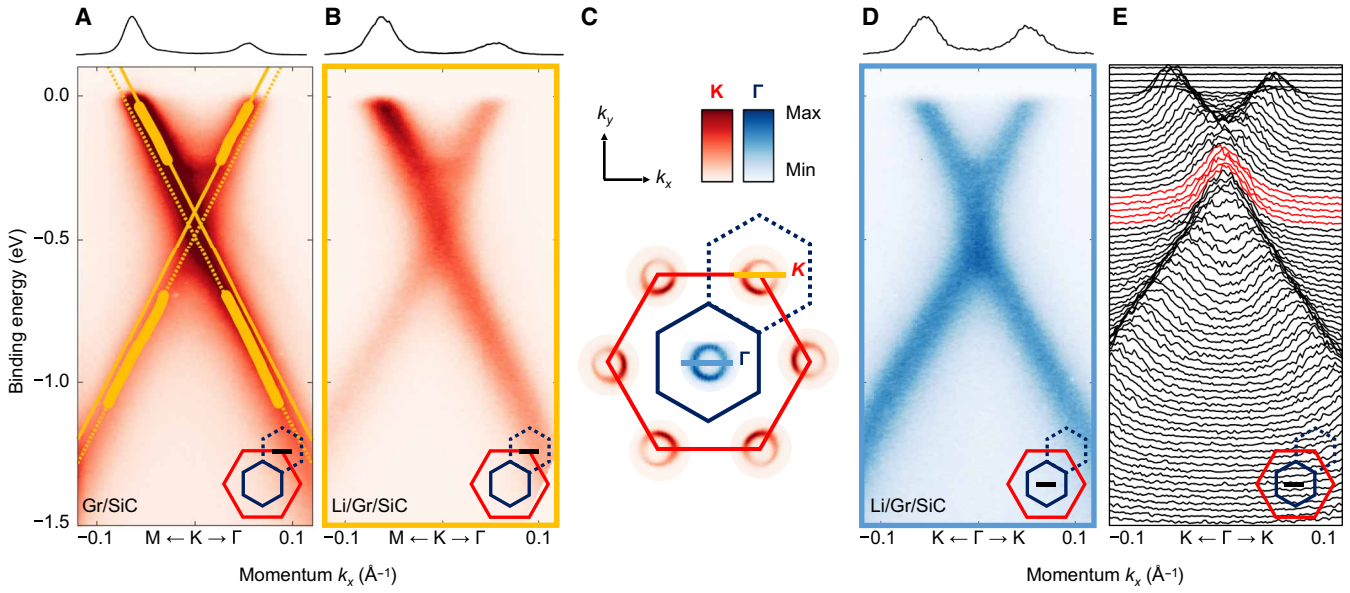

Fig. 2. Lithium-induced Kekulé bond DW formation in graphene. (**A**) ARPES spectra of pristine graphene on SiC through the Dirac cone at K [cut indicated by yellow line in (C)]. The Dirac cone displays electron doping due to charge transfer from the substrate, and one branch appears brighter due to matrix element effects. This is shown in the MDC at the Fermi level (top). MDC peak positions are indicated by thick yellow lines; linear fits through the top (solid lines) and bottom (dotted lines) indicate the presence of an energy gap (see text). (**B**) The same spectra as (A) after dilute Li deposition. No charge transfer doping from Li is detectable. (**C**) Schematic of the BZs of pristine graphene (red) and $(\sqrt{3} \times \sqrt{3})R30^\circ$ Kekulé graphene (blue) superimposed on the Fermi surfaces as observed by ARPES (not to scale, see fig. S11). Locations of the ARPES cuts in (A) and (B) and (D) and (E) are indicated by the yellow and blue lines, respectively. (**D**) ARPES spectra at **Γ** [cut indicated by blue line in (C)] after lithium deposition. The two Dirac cones at K/K′ are folded to **Γ**. Both branches are equally bright, indicating the mixed K/K′ character of the bands as shown in the Fermi level MDC (top). (**E**) MDCs of the spectra shown in (D). Fits to MDC curves reveal an energy gap at the Dirac point (see the Supplementary Materials). The spectra in red lie inside the gap region.

not crucial to our findings, and in either picture, our results are qualitatively the same. To extract energy gap values, we use the sublattice symmetry breaking picture, which allows us to model our experimental data with a simple tight-binding Hamiltonian (see the Supplementary Materials). This analysis yields an energy gap of $2\Delta = (292 \pm 4)$ meV at the Dirac point. For pristine graphene near E_F, there is no ARPES intensity at Γ, the BZ center.

Having confirmed the electronic structure for pristine graphene, we next decorate its surface with Li adatoms. Because of electron charge transfer from Li, the Dirac point is expected to shift downward in binding energy with increased Li concentration (*31*–*33*, *56*) (see the Supplementary Materials). However, we observe only a negligible shift of the Dirac point (below our 20-meV energy resolution), as shown by a direct comparison of ARPES intensity before (Fig. 2A) and after (Fig. 2B) Li deposition. We conclude that an extremely low Li surface coverage is achieved, with a conservative estimate of less than 0.3%, corresponding to an average Li-Li distance of ≥2 nm (see Materials and Methods). Despite this negligible change in charge density, we observe that the measured energy gap at the Dirac point increases by 20% to $2\Delta' = 354 \pm 2$ meV. Since Li adatoms occupy graphene sublattice symmetric hollow sites (Fig. 1E) (*31*), Li cannot further break A-B sublattice symmetry. In addition, this gap enhancement after ultralow 0.3% Li deposition cannot be explained by electron-plasmon effects (see the Supplementary Materials). As we will show below, we attribute this increased gap to the onset of Kekulé DW order. From Eq. 1, Dirac point energy gaps from concomitant sublattice symmetry breaking and Kekulé order add in quadrature, $2\Delta' = 2\sqrt{\Delta_{AB}^2 + \Delta_K^2}$, which in our measurements corresponds to $2\Delta_K \approx 200$ meV. More notable, and the primary signature of Kekulé order, is the appearance of new electronic energy bands centered at the Γ point and directly observed in Fermi surface maps (Fig. 2C). These new bands appear as a replica Dirac cone (Fig. 2D), which we interpret as the Kekulé-induced superposition of folded Dirac cones at K and K′, as in Fig. 1D. This is supported by the momentum-symmetric intensity of the Dirac cone centered at Γ (Fig. 2D), which reflects its mixed K/K′ character (Fig. 2B) because of contributions from Dirac cones at opposite ends of the graphene BZ (Fig. 2C, red hexagon). By performing a similar MDC analysis on this new Dirac cone at Γ, we extract a larger energy gap opening of $2\Delta' = 377 \pm 2$ meV in contrast to the gap observed at the BZ corner. One likely explanation for this discrepancy is the possible presence of minority areas of the sample with pristine, undistorted graphene that are measured by our ultraviolet light source (spot size, ~1 mm). While ARPES intensity at the Γ point originates exclusively from Kekulé-induced band folding and features a larger energy gap ($2\Delta' = 2\sqrt{\Delta_{AB}^2 + \Delta_K^2}$), the ARPES intensity measured at the K point contains signal from both Kekulé-distorted and possible undistorted graphene regions with smaller energy gap, $2\Delta' = 2\Delta_{AB}$.

Similar band folding and gap opening behavior has been observed in previous experiments where alkali atoms were intercalated into bilayer graphene at a high density (33% coverage or 100 times our estimated Li concentration) (*27*, *32*, *33*). However, in these experiments, band folding is naturally expected to occur owing to the presence of the uniform $(\sqrt{3} \times \sqrt{3})R30°$ adatom superlattice potential that explicitly breaks the global translational symmetry of graphene. The high adatom coverage also strongly electron-dopes graphene, resulting in a strong (~1 eV) downward shift of the Dirac point

binding energy ($E_D \sim -1.4$ eV) (*27*, *32*, *56*, *57*) and the appearance of alkali atom–derived electronic bands at Γ (*31*, *56*). We detect no such Dirac point shift or Li-derived bands. This also allows us to rule out the presence of rare islands of densely aggregated $(\sqrt{3} \times \sqrt{3})R30°$–ordered Li as such islands would similarly strongly locally dope graphene and thus produce replica Dirac cones at the Γ point with shifted Dirac point binding energies of ~ −1.4 eV. In contrast, our results are well explained by the global onset of an incipient and phase-coherent Kekulé DW instability driven by the long-range ordering of an extremely dilute (<0.3%) surface concentration of mobile Li adatoms (*45*, *46*). This is especially evidenced by the particular sharpness of the replica Dirac cone at Γ (Fig. 2, D and E) over the large spot size of our ultraviolet light source (~1 mm). This long-range phase coherence originates from a majority of mobile Li adatoms occupying a single-colored Kekulé site (Fig. 1H), and it is confirmed by temperature-dependent measurements (up to 30 K), which found that the folded Γ-point Dirac bands unexpectedly sharpen further as the sample is warmed, indicative of increased hidden Kekulé order as more single-colored Kekulé sites are populated by mobile Li adatoms (see the Supplementary Materials). Notably, while natural point defects have been shown to nucleate DW order in bulk materials (*58*, *59*), this is the first controlled demonstration of dilute extrinsic adatoms inducing a global DW phase in a two-dimensional material.

We note that such direct signatures of DW order in monolayer graphene are rare (*23*, *26*, *28*). As DW order is concomitant with a periodic lattice distortion (*1*), a Kekulé distortion of the graphene lattice (Fig. 1C) should be reflected in diffraction measurements. To further support our claim of a global Kekulé distorted phase, we performed in situ low-temperature low-energy electron diffraction (LEED) measurements (spot size, ~1 mm) (Fig. 3). Before Li deposition, the pristine surface displays sharp diffraction peaks characteristic of epitaxial graphene grown on SiC (Fig. 3A). After dilute Li deposition, new and sharp diffraction peaks appear corresponding to a well-defined and long-ranged $(\sqrt{3} \times \sqrt{3})R30°$ lattice (Fig. 3B). Relative to the atomic graphene Bragg peaks (red arrows, Fig. 3C), the new diffraction peaks (blue arrows, Fig. 3C) have intensities of ~20% with similar peak widths (see the Supplementary Materials). In light of the ultradilute surface coverage of Li adatoms (<0.3%), the intensity and sharpness of these new diffraction peaks point to the presence of a globally well-defined Kekulé lattice distortion in graphene.

We next present a simple model that captures how the emergence of Kekulé order depends on the two key control parameters in our study: sample temperature and Li deposition rate. In our experiments, we find that Kekulé order occurs only when (i) Li is deposited with graphene held at low temperature (<10 K) and (ii) Li is deposited at a slow rate. We use a kinetic hopping model that incorporates the graphene-mediated long-range interaction between Li adatoms on graphene (Fig. 1, E to H), which is attractive for Li located on Kekulé RGB lattices sites of the same "color" and repulsive otherwise (*45*, *46*) (see the Supplementary Materials for detailed discussion). In the model (Fig. 4A), Li can hop to neighboring sites with a Boltzmann probability dependent on temperature and the local Kekulé-modulated potential energy landscape created by all other surface Li atoms (Fig. 4C). We quantify the strength of RGB Kekulé order in the system by calculating the magnitude of the $(\sqrt{3} \times \sqrt{3})R30°$ Fourier component of the Li lattice positions. In agreement with our findings, slower Li deposition (Fig. 4A) produces coherent long-range Kekulé order across the entire sample, while faster deposition (Fig. 4B) only permits order on the scale of a few sites. By performing several simulations with varying temperatures and deposition rates (Fig. 4D), we find that long-range Kekulé ordering does not form at high sample temperatures. The unique combination of slow deposition at low temperature in our experiments may explain why Kekulé order in dilute Li graphene systems has not been reported previously (*56*). However, starting from the ordered phase, higher temperature can initially improve long-range Kekulé order via increased

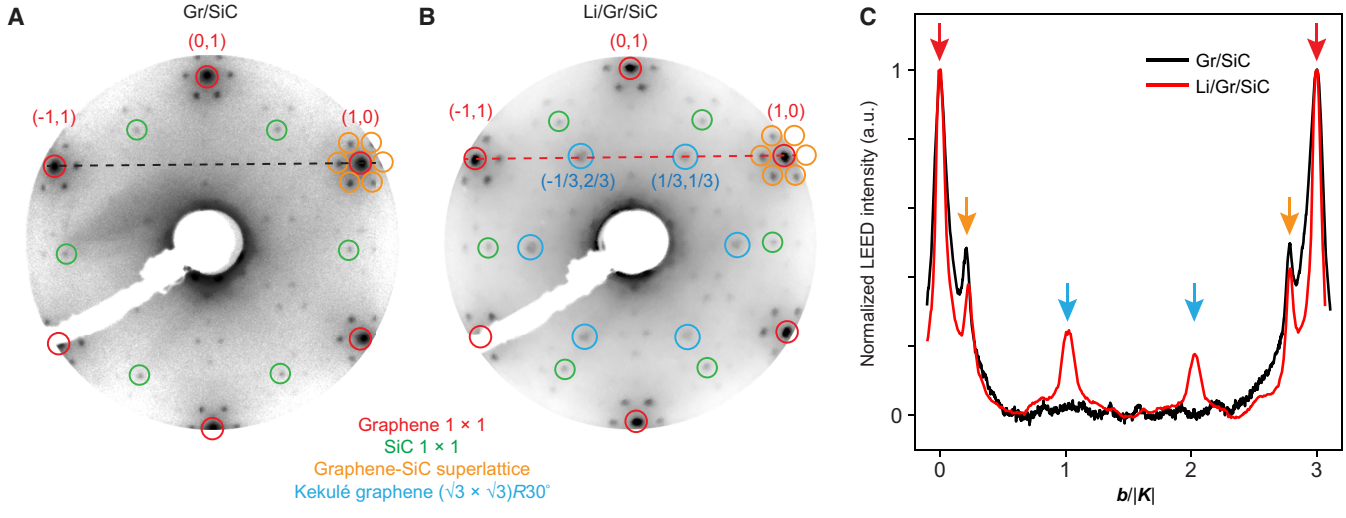

Fig. 3. LEED of graphene in the Kekulé phase. (**A**) LEED pattern measured at 66 eV on pristine Gr/SiC. Peaks are highlighted with circles corresponding to graphene (red), SiC (green), and the graphene/SiC superlattice pattern (yellow). (**B**) LEED pattern after dilute lithium deposition at low temperature. New diffraction spots corresponding to $(\sqrt{3} \times \sqrt{3})R30°$ Kekulé bond order (blue) are clearly visible. (**C**) Line profiles along the black (red) dotted line in (A) [(B)] after subtraction of a smooth background (see the Supplementary Materials). The horizontal axis is in units of the K-point wave vector, $|K| = 1.70$ Å^{-1}. a.u., arbitrary units. Diffraction peaks are indicated by arrows using the same color scheme used in (B). The width of the graphene and graphene/SiC peaks are comparable before and after Li deposition. The new Kekulé diffraction peaks (blue arrows) are intense (~20%) and as sharp as the graphene Bragg peaks (red arrows), indicating long-range Kekulé bond order.

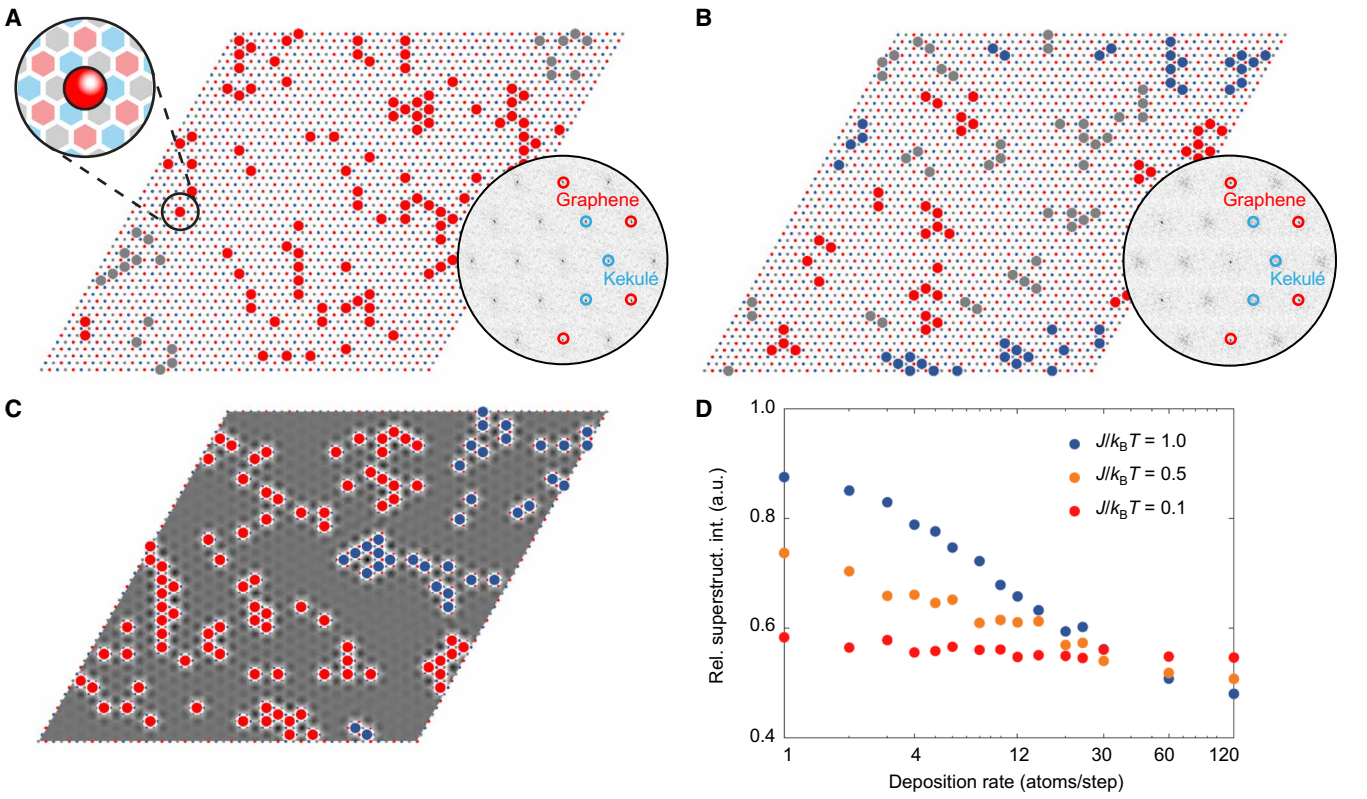

Fig. 4. Kinetic model for hidden Kekulé ordering of Li. (**A**) Simulation of 120 adatoms (large dots) added randomly one at a time (slow deposition) to RGB hollow sites that form three $(\sqrt{3} \times \sqrt{3})R30°$ mosaic Kekulé lattices on graphene. After each Li is added, the adatoms interact through a long-range "ferromagnetic"-like potential, and the system is evolved thermally (see the Supplementary Materials). The formation of a large unicolor (red) Kekulé order is observed. Left inset: Zoom view. Right inset: Fourier transform of the simulation, with sharp peaks at the $(\sqrt{3} \times \sqrt{3})R30°$ Kekulé ordering wave vector signifying long-range order. (**B**) Final state of a similar simulation when adatoms are added in a single step (fast deposition) and allowed to evolve thermally. Unicolor patches are much smaller than those from slow deposition in (A), and the Kekulé peaks in the Fourier transform are broadened, signifying short-range order. (**C**) Simulated potential energy landscape originating from the superposition of $(\sqrt{3} \times \sqrt{3})R30°$ Friedel oscillations from all adatoms. The egg carton–like potential is deepest (dark) near large unicolor regions, where mobile adatoms can become "trapped" and further enhance the Kekulé order. (**D**) Intensity of the Fourier peak corresponding to the $(\sqrt{3} \times \sqrt{3})R30°$ Kekulé lattice (normalized by the intensity at the graphene Bragg peak) as a function of adatom deposition rate, for different values of J/k_BT, where J is the adatom-adatom interaction coupling constant (see the Supplementary Materials), k_B is the Boltzmann constant, and T is temperature. At low temperatures ($J/k_BT \geq 1$), Kekulé order is strongest for slow adatom deposition; at high temperatures ($J/k_BT \ll 1$), Kekulé order is weak at any deposition rate.

Li mobility (fig. S12) until the kinetic energy eclipses the Kekulé-confining potential (Fig. 4C), whence Li hopping becomes random and destroys the ordered phase (see the Supplementary Materials).

DISCUSSION

Thus far, our results are well explained by the predictions of hidden Kekulé ordering of adatoms (*45*, *46*). However, a key parameter for long-range Li order is the graphene electronic doping level: At finite charge density, the Fermi surface transitions from point-like to ring-like, and additional long wavelength Friedel oscillations of magnitude $2k_F$ (called intravalley scattering) (*43*, *46*–*48*) contribute to the total electron scattering wave vector, which disrupts the perfect nesting condition (figs. S8 and S11), $\delta\boldsymbol{q} = \boldsymbol{K} - \boldsymbol{K}' + 2\boldsymbol{k}_F$. The intravalley contribution has a long spatial period given by $2\pi/2k_F = \lambda_F/2 = \sqrt{\pi/n_e}$, which modulates the short wavelength ($\lambda_{\Delta K} = 4.26$ Å) intervalley oscillations that are commensurate with the Kekulé lattice (fig. S8). When the charge density, n_e, becomes as large as the surface density of Li adatoms that nucleate the local Kekulé order, $n_e \geq n_{Li}$, the $2k_F$ charge modulations effectively randomize the sign of the adatom interaction potential, V_{ij}, between adatoms at the mean Li-Li nearest-neighbor distance $\ell_{Li} \gtrsim 1/k_F$ (fig. S8) (*45*, *46*). Large charge densities are thus expected to destroy any long-range Li order, preventing the formation of a global, phase-coherent Kekulé distortion.

Unexpectedly, we find that the Kekulé order we observe in Gr/SiC (Figs. 2 and 3) occurs at an electronic density larger than the lithium density ($n_e \approx 1.4 \times 10^{13}$ cm^{-2} $\approx 2.3n_{Li}$), where ordering is not expected to occur. To further test the predicted deleterious effect of electronic density on Kekulé DW formation, we measured two additional epitaxial monolayer graphene samples with different doping levels (Fig. 5). Photoemission spectra from hydrogen (H)– and gadolinium (Gd)–intercalated graphene-SiC measured at the graphene K point are shown in Fig. 5 (A and C, respectively). The H-intercalated sample (Gr/H/SiC) is p doped (*60*), with the Dirac point shifted to ~100 meV above E_F ($n_h \approx 7.3 \times 10^{11}$ cm^{-2}), while the Gd-intercalated sample (Gr/Gd/SiC) is strongly n doped (*57*) with the Dirac point shifted to ~1.6 eV below E_F ($n_e \approx 4.5 \times 10^{14}$ cm^{-2}) (*57*). Figure 5 (B and D) displays ARPES measurements at Γ after Li deposition at low temperature and low deposition rate. We again find signatures of Kekulé distortion–induced folded K/K′ Dirac cones at Γ.

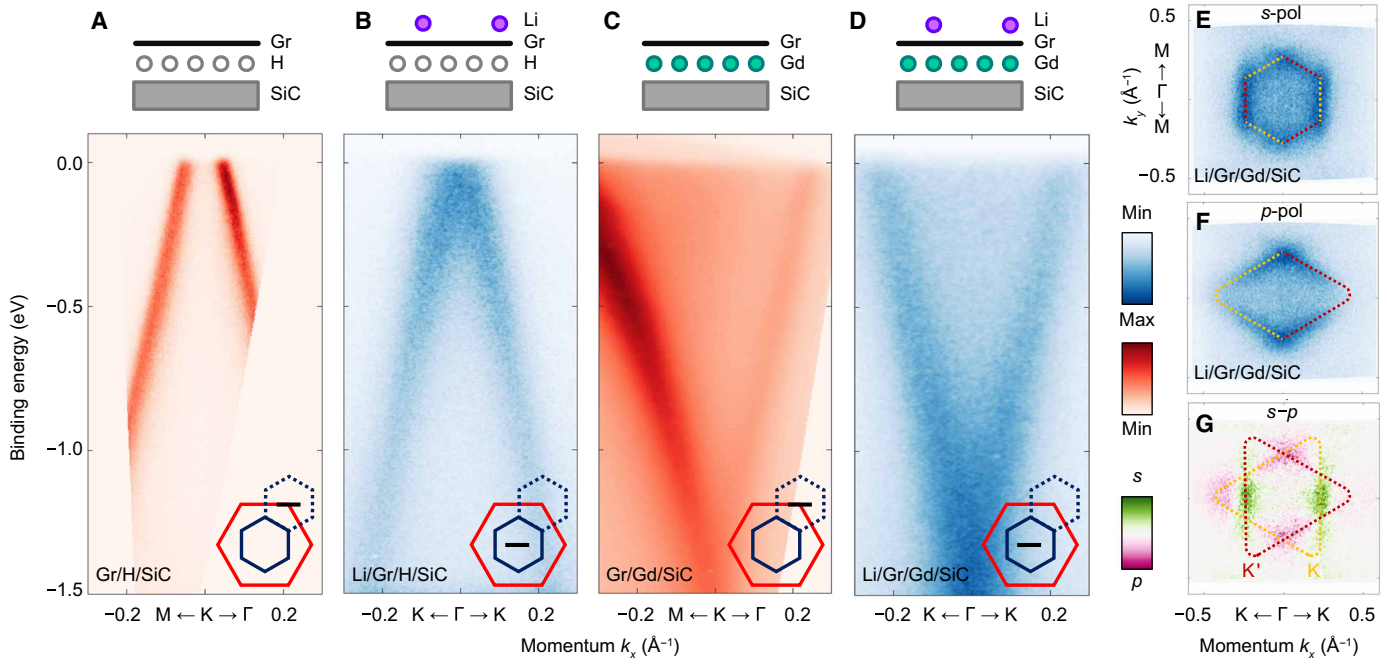

Fig. 5. Li-induced Kekulé phase in different graphene systems. (**A**) ARPES spectra taken at the K point (cut indicated by inset) on hydrogen-intercalated graphene (Gr/H/SiC) (sample schematic is shown above the cut). The Dirac point is located ~100 meV above E_F. (**B**) Spectra at Γ on Gr/H/SiC after lithium deposition showing the folded Dirac cone due to Kekulé distortion. (**C**) Spectra at K on gadolinium-intercalated graphene (Gr/Gd/SiC). Graphene is strongly doped with the Dirac point located ~1.6 eV below E_F. (**D**) Spectra at Γ on Gr/Gd/SiC after lithium deposition showing the folded Dirac cone. The folded Dirac cones in (B) and (D) display bands with symmetric intensities, signifying a folding of the two Dirac cones at K/K′. (**E**) Fermi surface of Gr/Gd/SiC at Γ after Li deposition using *s*-polarized light. A schematic of the bands expected to be visible in this configuration is overlaid in yellow and red dotted lines. (**F**) The same Fermi surface as in (E) using *p*-polarized light. (**G**) Difference map between (E) and (F). A schematic of the trigonal-warped Fermi surfaces folded from K and K′ is overlaid in yellow (K) and red (K′) dotted lines.

The folded nature of the bands is especially apparent for Gr/Gd/SiC at ultrahigh electron density, where we can directly visualize different portions of the trigonal-warped Fermi surface using different light polarizations (*61*) (Fig. 5, E to G). No ARPES intensity is present at Γ before Li deposition.

Despite significant differences in the size and carrier type of the Fermi surfaces, we observe signatures of Li-induced Kekulé distortion across all three graphene systems. While understanding the microscopic origin of this Kekulé ordering and its robustness to variation in the electron density will require more theoretical work, the role of electronic Fermi surface nesting in the global lattice distortion can be tentatively ruled out. An alternative, promising mechanism is momentum-dependent electron-phonon coupling, which has been found to drive lattice distortions in other two-dimensional systems (*6*, *7*); electron-phonon coupling is strong in graphene and especially so for the K-point A_1' "breathing" mode phonon (*9*–*11*), which has the exact symmetry as the Kekulé distortion (Fig. 1C) and its dispersion, $\Omega_{A_1'}(\boldsymbol{q})$, displays a strong renormalization (Kohn anomaly) at the Kekulé wave vector. This hypothesis could be further explored via time-resolved ARPES experiments, which can extract the mode-projected electron-coupling value (*11*) before and after the Kekulé distortion is induced.

Kekulé order and other coherent valley-coupled states have been theorized (*37*–*41*, *62*) to explain the correlated insulating and superconducting states in magic angle twisted bilayer graphene (*63*–*65*). However, a microscopic origin of the proposed global intervalley coupling is yet to be determined. Detailed phonon calculations on relaxed twisted bilayer structures showed that localized Kekulé order can emerge near moiré AA stacking sites, opening unexpectedly large gaps in the flat band energy spectrum (*62*). Defect-induced global Kekulé distortion may thus provide a plausible microscopic mechanism for the valley coupling in twisted bilayer graphene. Our results show that even an extremely dilute concentration of atomic-scale defects can initiate the global onset of an incipient DW instability in pristine monolayer graphene.

MATERIALS AND METHODS

Sample preparation

Pristine monolayer graphene (Gr/SiC) samples are grown epitaxially on hydrogen-etched silicon carbide [SiC(0001)] substrates in a radio frequency-heated furnace under argon atmosphere (*50*). Hydrogen intercalated samples (Gr/H/SiC) were prepared by annealing in molecular hydrogen at a pressure close to 1 bar and temperatures around 800°C. Gd-intercalated samples (Gr/Gd/SiC) were prepared by a procedure described in (*57*). Before ARPES measurements, the sample surface is cleaned by annealing at 600°C in ultrahigh vacuum for several hours and allowed to cool. Lithium is deposited in situ between 5 and 20 K using a commercial SAES alkali metal source over ~3 to 30 min at low deposition rate, as determined by the negligible shift in the graphene Dirac point.

Estimate of Li surface coverage

The charge density in doped graphene is given by $n_e = E_D^2/(\pi\hbar^2 v_F^2)$, where E_D is the Dirac point binding energy in ARPES measurements, $\hbar$ is Planck's constant divided by 2π, and v_F is the Fermi velocity.

After Li deposition, owing to a charge transfer of α free electrons per Li adatom, the Dirac point energy shifts to E_D', and the new charge density, n_e', is given by $n_e' = n_e + \alpha n_{Li} = (E_D')^2/(\pi\hbar^2 v_F^2)$, where n_{Li} is the density of Li adatoms and we assume that v_F is unchanged for low Li densities. Solving for n_{Li}, we arrive at

$$n_{Li} = \frac{(E_D')^2 - E_D^2}{\alpha\pi\hbar^2 v_F^2}$$

Previous experiments (*27*, *32*, *56*) on $(\sqrt{3}\times\sqrt{3})R30°$–ordered Li adatoms (one-third monolayer coverage) on Gr/SiC have reported a significant electron doping of graphene. The observed shifts in the Dirac point energy after Li deposition, $E_D' - E_D \sim 1000$ meV, allow us to estimate the coverage in our Li/Gr/SiC system where any possible shift is undetected within our energy resolution (~20 meV). From the reported Dirac point shifts and the Li density given by 1 Li per $(\sqrt{3}\times\sqrt{3})R30°$ supercell, one can estimate that each Li adatom contributes $\alpha \approx 0.2$ free electrons to graphene, in good agreement with ab initio calculations (*31*). In our estimate of the Li coverage, we assume this same value for α. Although we detect no shift in the Dirac point after Li deposition, we can arrive at a conservative upper bound from our energy resolution of 20 meV, $E_D' < E_D + 20$ meV = 450 meV. Using $E_D' < 450$ meV, $E_D = 430$ meV, and $\alpha \approx 0.2$, we estimate a dilute Li density of $n_{Li} < 6\times10^{12}$ cm^{-2}. This Li density corresponds to a surface coverage of <0.3% and an average Li-Li distance of $\ell_{Li} = (\pi n_{Li})^{-1/2} \geq 2$ nm, which is on the order of the radial size of the local intervalley scattering pattern of ~2 to 5 nm (*47*). Notably, this estimated Li density is similar to that of point defect–mediated DW formation in the α phase of Sn/Ge(111) (*58*) and is four times more dilute than a similar defect-induced Kekulé distortion reported previously (1.3% or $n_{defect} = 23.6\times10^{12}$ cm^{-2}) (*23*).

Kekulé Hamiltonian

The Hamiltonian for pristine graphene is given by the 4 × 4 valley- and sublattice-isospin matrix

$$\mathcal{H}_0 = \hbar v_F \hat{\tau}_z \otimes (\boldsymbol{\sigma}\cdot\boldsymbol{k}) = \begin{pmatrix} \hbar v_F \boldsymbol{\sigma}\cdot\boldsymbol{k} & \mathbf{0}_2 \\ \mathbf{0}_2 & -\hbar v_F \boldsymbol{\sigma}\cdot\boldsymbol{k} \end{pmatrix} \quad (2)$$

expressed in the (ψ_{AK}, ψ_{BK}, $\psi_{BK'}$, $\psi_{AK'}$) basis and where $\hbar$ is Planck's constant divided by 2π, v_F is the graphene Fermi velocity, $\hat{\tau}_i$ and $\hat{\sigma}_i$ are Pauli matrices that act on the valley- and sublattice-isospin degrees of freedom, respectively, and $\hat{\sigma}_0$ ($\hat{\tau}_0$) is the sublattice (valley) (2 × 2) identity matrix, ⊗ is the direct (or tensor) product, and $\mathbf{0}_2$ is a 2 × 2 matrix of zeros.

In this basis, the sublattice symmetry breaking term is given by the matrix (*25*, *36*)

$$\mathcal{H}_{AB} = \Delta_{AB}\hat{\tau}_z \otimes \hat{\sigma}_z = \begin{pmatrix} \Delta_{AB}\hat{\sigma}_z & \mathbf{0}_2 \\ \mathbf{0}_2 & -\Delta_{AB}\hat{\sigma}_z \end{pmatrix} \quad (3)$$

where Δ_{AB} is the difference in on-site energies on the A and B graphene sublattices.

The Kekulé distortion breaks valley symmetry by coupling the K and K′ valley block off-diagonal subspaces in the pristine graphene Hamiltonian in Eq. 2. The Kekulé-O gap term, Δ_K, opens a real energy gap ($2|\Delta_K|$), although it is, in general, complex valued ($\Delta_K = |\Delta_K| e^{i\varphi}$) with a magnitude ($|\Delta_K|$) related to the change in bond hopping energy and a phase ($e^{i\varphi}$) related to the bond distortion pattern (*13*–*15*, *30*) and is given by the matrix (*14*–*16*, *25*, *36*)

$$\mathcal{H}_K = (|\Delta_K|\cos\varphi\,\hat{\tau}_x - |\Delta_K|\sin\varphi\,\hat{\tau}_y)\otimes\sigma_0 = \begin{pmatrix} \mathbf{0}_2 & \Delta_K\hat{\sigma}_0 \\ \widetilde{\Delta}_K\hat{\sigma}_0 & \mathbf{0}_2 \end{pmatrix} \quad (4)$$

where $\widetilde{\Delta}_K$ is the complex conjugate of Δ_K.

The total Hamiltonian that allows for both an A-B sublattice symmetry breaking term, Δ_{AB}, and Kekulé distortion term, Δ_K, is given by

$$\mathcal{H} = \mathcal{H}_0 + \mathcal{H}_{AB} + \mathcal{H}_K = \begin{pmatrix} \hbar v_F \boldsymbol{\sigma}\cdot\boldsymbol{k} + \Delta_{AB}\hat{\sigma}_z & \Delta_K\hat{\sigma}_0 \\ \widetilde{\Delta}_K\hat{\sigma}_0 & -\hbar v_F \boldsymbol{\sigma}\cdot\boldsymbol{k} - \Delta_{AB}\hat{\sigma}_z \end{pmatrix} \quad (5)$$

expressed in the (ψ_{AK}, ψ_{BK}, $\psi_{BK'}$, $\psi_{AK'}$) basis. The energy eigenvalues for this Hamiltonian are given by Eq. 1. Together, the sublattice and Kekulé terms open an energy gap at the Dirac point of total size (*25*)

$$2\Delta' = 2\sqrt{\Delta_{AB}^2 + \Delta_K^2} \quad (6)$$

ARPES/LEED measurements

ARPES and LEED experiments were performed at the University of British Columbia in an ultrahigh vacuum chamber equipped with a SPECS Phoibos 150 Hemispherical Analyzer, a SPECS UVS300 Monochromatized Gas Discharge Lamp, and a SPECS ErLEED 1000A. The sample temperature was held between 5 and 30 K for all experiments, and the chamber pressure was better than 5×10^{-11} torr. For the ARPES experiments, *s*- and *p*-polarized 21.2-eV photons were used, and the energy and momentum resolution were better than 20 meV and 0.01 Å^{-1}, respectively.

SUPPLEMENTARY MATERIALS

Supplementary material for this article is available at https://science.org/doi/10.1126/sciadv.abm5180

REFERENCES AND NOTES

1. G. Grüner, *Density Waves in Solids* (Addison-Wesley, 1994).
2. D. E. Moncton, J. D. Axe, F. J. DiSalvo, Neutron scattering study of the charge-density wave transitions in 2*H*–$TaSe_2$ and 2*H*–$NbSe_2$. *Phys. Rev. B* **16**, 801–819 (1977).
3. J. Tranquada, B. Sternlieb, J. Axe, Y. Nakamura, S. Uchida, Evidence for stripe correlations of spins and holes in copper oxide superconductors. *Nature* **375**, 561–563 (1995).
4. B. Sipos, A. F. Kusmartseva, A. Akrap, H. Berger, L. Forró, E. Tutiš, From Mott state to superconductivity in 1T-TaS_2. *Nat. Mater.* **7**, 960–965 (2008).
5. R. E. Peierls, *Quantum Theory of Solids* (Clarendon Press, 1956).
6. M. D. Johannes, I. I. Mazin, Fermi surface nesting and the origin of charge density waves in metals. *Phys. Rev. B* **77**, 165135 (2008).
7. F. Weber, S. Rosenkranz, J.-P. Castellan, R. Osborn, R. Hott, R. Heid, K.-P. Bohnen, T. Egami, A. H. Said, D. Reznik, Extended phonon collapse and the origin of the charge-density wave in 2*H*–$NbSe_2$. *Phys. Rev. Lett.* **107**, 107403 (2011).
8. X. Zhu, Y. Cao, J. Zhang, E. Plummer, J. Guo, Classification of charge density waves based on their nature. *Proc. Natl. Acad. Sci.* **112**, 2367–2371 (2015).
9. S. Piscanec, M. Lazzeri, F. Mauri, A. C. Ferrari, J. Robertson, Kohn anomalies and electron-phonon interactions in graphite. *Phys. Rev. Lett.* **93**, 185503 (2004).
10. S. Y. Zhou, D. A. Siegel, A. V. Fedorov, A. Lanzara, Kohn anomaly and interplay of electron-electron and electron-phonon interactions in epitaxial graphene. *Phys. Rev. B* **78**, 193404 (2008).
11. M. X. Na, A. K. Mills, F. Boschini, M. Michiardi, B. Nosarzewski, R. P. Day, E. Razzoli, A. Sheyerman, M. Schneider, G. Levy, S. Zhdanovich, T. P. Devereaux, A. F. Kemper, D. J. Jones, A. Damascelli, Direct determination of mode-projected electron-phonon coupling in the time domain. *Science* **366**, 1231–1236 (2019).
12. T. Tudorovskiy, S. A. Mikhailov, Intervalley plasmons in graphene. *Phys. Rev. B* **82**, 073411 (2010).
13. C. Chamon, Solitons in carbon nanotubes. *Phys. Rev. B* **62**, 2806–2812 (2000).

14. C.-Y. Hou, C. Chamon, C. Mudry, Electron fractionalization in two-dimensional graphenelike structures. *Phys. Rev. Lett.* **98**, 186809 (2007).
15. K. Nomura, S. Ryu, D.-H. Lee, Field-induced Kosterlitz-Thouless transition in the N = 0 Landau level of graphene. *Phys. Rev. Lett.* **103**, 216801 (2009).
16. I. F. Herbut, V. Juričić, B. Roy, Theory of interacting electrons on the honeycomb lattice. *Phys. Rev. B* **79**, 085116 (2009).
17. C. Weeks, M. Franz, Interaction-driven instabilities of a Dirac semimetal. *Phys. Rev. B* **81**, 085105 (2010).
18. A. V. Balatsky, Peierls instability and chiral-symmetry breaking in solids with "relativistic" fermions. *Phys. Rev. Lett.* **64**, 2078–2081 (1990).
19. J. W. Mintmire, B. I. Dunlap, C. T. White, Are fullerene tubules metallic? *Phys. Rev. Lett.* **68**, 631–634 (1992).
20. K. K. Gomes, W. Mar, W. Ko, F. Guinea, H. C. Manoharan, Designer Dirac fermions and topological phases in molecular graphene. *Nature* **483**, 306–310 (2012).
21. M. Koshino, T. Morimoto, M. Sato, Topological zero modes and Dirac points protected by spatial symmetry and chiral symmetry. *Phys. Rev. B* **90**, 115207 (2014).
22. Y. Ren, X. Deng, Z. Qiao, C. Li, J. Jung, C. Zeng, Z. Zhang, Q. Niu, Single-valley engineering in graphene superlattices. *Phys. Rev. B* **91**, 245415 (2015).
23. C. Gutierrez, C.-J. Kim, L. Brown, T. Schiros, D. Nordlund, E. B. Lochocki, K. M. Shen, J. Park, A. N. Pasupathy, Imaging chiral symmetry breaking from Kekulé bond order in graphene. *Nat. Phys.* **12**, 950–958 (2016).
24. O. V. Gamayun, V. P. Ostroukh, N. V. Gnezdilov, I. Adagideli, C. W. J. Beenakker, Valley-momentum locking in a graphene superlattice with Y-shaped Kekulé bond texture. *New J. Phys.* **20**, 023016 (2018).
25. S. Ryu, C. Mudry, C.-Y. Hou, C. Chamon, Masses in graphenelike two-dimensional electronic systems: Topological defects in order parameters and their fractional exchange statistics. *Phys. Rev. B* **80**, 205319 (2009).
26. S.-Y. Li, Y. Zhang, L.-J. Yin, L. He, Scanning tunneling microscope study of quantum Hall isospin ferromagnetic states in the zero Landau level in a graphene monolayer. *Phys. Rev. B* **100**, 085437 (2019).
27. C. Bao, H. Zhang, T. Zhang, X. Wu, L. Luo, S. Zhou, Q. Li, Y. Hou, W. Yao, L. Liu, P. Yu, J. Li, W. Duan, H. Yao, Y. Wang, S. Zhou, Experimental evidence of chiral symmetry breaking in Kekulé-ordered graphene. *Phys. Rev. Lett.* **126**, 206804 (2021).
28. X. Liu, G. Farahi, C.-L. Chiu, Z. Papic, K. Watanabe, T. Taniguchi, M. P. Zaletel, A. Yazdani, Visualizing broken symmetry and topological defects in a quantum Hall ferromagnet. *Science* **375**, 321–326 (2022).
29. L. Classen, M. M. Scherer, C. Honerkamp, Instabilities on graphene's honeycomb lattice with electron-phonon interactions. *Phys. Rev. B* **90**, 035122 (2014).
30. M. Kharitonov, Phase diagram for the ν=0 quantum Hall state in monolayer graphene. *Phys. Rev. B* **85**, 155439 (2012).
31. M. Farjam, H. Rafii-Tabar, Energy gap opening in submonolayer lithium on graphene: Local density functional and tight-binding calculations. *Phys. Rev. B* **79**, 045417 (2009).
32. K. Sugawara, K. Kanetani, T. Sato, T. Takahashi, Fabrication of Li-intercalated bilayer graphene. *AIP Adv.* **1**, 022103 (2011).
33. K. Kanetani, K. Sugawara, T. Sato, R. Shimizu, K. Iwaya, T. Hitosugi, T. Takahashi, Ca intercalated bilayer graphene as a thinnest limit of superconducting C6Ca. *Proc. Natl. Acad. Sci.* **109**, 19610–19613 (2012).
34. C. A. Marianetti, H. G. Yevick, Failure mechanisms of graphene under tension. *Phys. Rev. Lett.* **105**, 245502 (2010).
35. S.-H. Lee, H.-J. Chung, J. Heo, H. Yang, J. Shin, U.-I. Chung, S. Seo, Band gap opening by two dimensional manifestation of Peierls instability in graphene. *ACS Nano* **5**, 2964–2969 (2011).
36. V. Gusynin, S. Sharapov, J. Carbotte, AC conductivity of graphene: From tight-binding model to 2+1-dimensional quantum electrodynamics. *Int. J. Mod. Phys. B* **21**, 4611–4658 (2007).
37. X. Y. Xu, K. T. Law, P. A. Lee, Kekulé valence bond order in an extended Hubbard model on the honeycomb lattice with possible applications to twisted bilayer graphene. *Phys. Rev. B* **98**, 121406 (2018).
38. A. Thomson, S. Chatterjee, S. Sachdev, M. S. Scheurer, Triangular antiferromagnetism on the honeycomb lattice of twisted bilayer graphene. *Phys. Rev. B* **98**, 075109 (2018).
39. Y. Da Liao, Z. Y. Meng, X. Y. Xu, Valence bond orders at charge neutrality in a possible two-orbital extended Hubbard model for twisted bilayer graphene. *Phys. Rev. Lett.* **123**, 157601 (2019).
40. S.-M. Huang, Y.-P. Huang, T.-K. Lee, Slave-rotor theory on magic-angle twisted bilayer graphene. *Phys. Rev. B* **101**, 235140 (2020).
41. Y. Da Liao, J. Kang, C. N. Breiø, X. Y. Xu, H.-Q. Wu, B. M. Andersen, R. M. Fernandes, Z. Y. Meng, Correlation-induced insulating topological phases at charge neutrality in twisted bilayer graphene. *Phys. Rev. X* **11**, 011014 (2021).
42. A. Damascelli, Probing the electronic structure of complex systems by ARPES. *Phys. Scr.* **T109**, 61–74 (2004).
43. V. V. Cheianov, V. I. Fal'ko, Friedel oscillations, impurity scattering, and temperature dependence of resistivity in graphene. *Phys. Rev. Lett.* **97**, 226801 (2006).
44. C. Bena, Effect of a single localized impurity on the local density of states in monolayer and bilayer graphene. *Phys. Rev. Lett.* **100**, 076601 (2008).
45. V. V. Cheianov, V. I. Fal'ko, O. Syljuasen, B. L. Altshuler, Hidden Kekulé ordering of adatoms on graphene. *Solid State Commun.* **149**, 1499–1501 (2009).
46. V. V. Cheianov, O. Syljuasen, B. L. Altshuler, V. Fal'ko, Ordered states of adatoms on graphene. *Phys. Rev. B* **80**, 233409 (2009).
47. G. M. Rutter, J. Crain, N. Guisinger, T. Li, P. First, J. A. Stroscio, Scattering and interference in epitaxial graphene. *Science* **317**, 219–222 (2007).
48. P. Mallet, I. Brihuega, S. Bose, M. M. Ugeda, J. M. Gomez-Rodriguez, K. Kern, J.-Y. Veuillen, Role of pseudospin in quasiparticle interferences in epitaxial graphene probed by high-resolution scanning tunneling microscopy. *Phys. Rev. B* **86**, 045444 (2012).
49. C. Dutreix, H. González-Herrero, I. Brihuega, M. I. Katsnelson, C. Chapelier, V. T. Renard, Measuring the Berry phase of graphene from wavefront dislocations in Friedel oscillations. *Nature* **574**, 219–222 (2019).
50. S. Forti, U. Starke, Epitaxial graphene on SiC: From carrier density engineering to quasi-free standing graphene by atomic intercalation. *J. Phys. D Appl. Phys.* **47**, 094013 (2014).
51. S. Y. Zhou, G.-H. Gweon, A. V. Fedorov, P. N. First, W. A. de Heer, D.-H. Lee, F. Guinea, A. H. C. Neto, A. Lanzara, Substrate-induced bandgap opening in epitaxial graphene. *Nat. Mater.* **6**, 770–775 (2007).
52. A. Bostwick, T. Ohta, T. Seyller, K. Horn, E. Rotenberg, Quasiparticle dynamics in graphene. *Nat. Phys.* **3**, 36–40 (2007).
53. I. Gierz, J. Henk, H. Höchst, C. R. Ast, K. Kern, Illuminating the dark corridor in graphene: Polarization dependence of angle-resolved photoemission spectroscopy on graphene. *Phys. Rev. B* **83**, 121408 (2011).
54. P. Nigge, A. C. Qu, E. Lantagne-Hurtubise, E. Marsell, S. Link, G. Tom, M. Zonno, M. Michiardi, M. Schneider, S. Zhdanovich, G. Levy, U. Starke, C. Gutiérrez, D. Bonn, S. A. Burke, M. Franz, A. Damascelli, Room temperature strain-induced Landau levels in graphene on a wafer-scale platform. *Science Advances* **5**, eaaw5593 (2019).
55. A. Bostwick, F. Speck, T. Seyller, K. Horn, M. Polini, R. Asgari, A. H. MacDonald, E. Rotenberg, Observation of plasmarons in quasi-freestanding doped graphene. *Science* **328**, 999–1002 (2010).
56. B. M. Ludbrook, G. Levy, P. Nigge, M. Zonno, M. Schneider, D. J. Dvorak, C. N. Veenstra, S. Zhdanovich, D. Wong, P. Dosanjh, C. Straßer, A. Stöhr, S. Forti, C. R. Ast, U. Starke, A. Damascelli, Evidence for superconductivity in Li-decorated monolayer graphene. *Proc. Natl. Acad. Sci. U.S.A.* **112**, 11795–11799 (2015).
57. S. Link, S. Forti, A. Stöhr, K. Küster, M. Rösner, D. Hirschmeier, C. Chen, J. Avila, M. C. Asensio, A. A. Zakharov, T. O. Wehling, A. I. Lichtenstein, M. I. Katsnelson, U. Starke, Introducing strong correlation effects into graphene by gadolinium intercalation. *Phys. Rev. B* **100**, 121407 (2019).
58. A. V. Melechko, J. Braun, H. H. Weitering, E. W. Plummer, Two-dimensional phase transition mediated by extrinsic defects. *Phys. Rev. Lett.* **83**, 999–1002 (1999).
59. C. J. Arguello, S. P. Chockalingam, E. P. Rosenthal, L. Zhao, C. Gutierrez, J. H. Kang, W. C. Chung, R. M. Fernandes, S. Jia, A. J. Millis, R. J. Cava, A. N. Pasupathy, Visualizing the charge density wave transition in 2*H*-$NbSe_2$ in real space. *Phys. Rev. B* **89**, 235115 (2014).
60. C. Riedl, C. Coletti, T. Iwasaki, A. A. Zakharov, U. Starke, Quasi-free-standing epitaxial graphene on SiC obtained by hydrogen intercalation. *Phys. Rev. Lett.* **103**, 246804 (2009).
61. S. W. Jung, S. H. Ryu, W. J. Shin, Y. Sohn, M. Huh, R. J. Koch, C. Jozwiak, E. Rotenberg, A. Bostwick, K. S. Kim, Black phosphorus as a bipolar pseudospin semiconductor. *Nat. Mater.* **19**, 277–281 (2020).
62. M. Angeli, E. Tosatti, M. Fabrizio, Valley Jahn-Teller effect in twisted bilayer graphene. *Phys. Rev. X* **9**, 041010 (2019).
63. Y. Cao, V. Fatemi, A. Demir, S. Fang, S. L. Tomarken, J. Y. Luo, J. D. Sanchez-Yamagishi, K. Watanabe, T. Taniguchi, E. Kaxiras, R. C. Ashoori, P. Jarillo-Herrero, Correlated insulator behaviour at half-filling in magic-angle graphene superlattices. *Nature* **556**, 80–84 (2018).
64. Y. Cao, V. Fatemi, S. Fang, K. Watanabe, T. Taniguchi, E. Kaxiras, P. Jarillo-Herrero, Unconventional superconductivity in magic-angle graphene superlattices. *Nature* **556**, 43–50 (2018).
65. L. Balents, C. R. Dean, D. K. Efetov, A. F. Young, Superconductivity and strong correlations in moiré flat bands. *Nat. Phys.* **16**, 725–733 (2020).

Acknowledgments: We acknowledge useful discussions with J. H. Smet, A. Kogar, R. M. Fernandes, Z.-B. Kang, and I. F. Herbut. **Funding:** This research was undertaken thanks in part to funding from the Max Planck-UBC-UTokyo Centre for Quantum Materials and the Canada First Research Excellence Fund, Quantum Materials and Future Technologies Program. The work at UBC was supported by the Killam, Alfred P. Sloan, and Natural Sciences and Engineering Research Council of Canada's (NSERC's) Steacie Memorial Fellowships (A.D.), the Alexander von Humboldt Fellowship (A.D.), the Canada Research Chairs Program (A.D.), NSERC, Canada Foundation for Innovation (CFI), British Columbia Knowledge Development Fund (BCKDF), and the CIFAR Quantum Materials Program. Work at MPI Stuttgart was supported by the German Research

Foundation (DFG) in the framework of the Priority Program No. 1459, Graphene (Sta315/8-2).
Author contributions: A.C.Q. and P.N. performed the ARPES and LEED experiments and analyzed the ARPES data. S.L. and U.S. grew all graphene samples. A.C.Q. performed tight binding calculations. A.C.Q. developed the thermal atomic hopping model and performed calculations with assistance from T.M. P.L.S. and C.G. analyzed LEED data. A.C.Q., P.N., M.M., M.S., S.Z., and G.L. provided technical support and maintenance for the ARPES setup. C.G. and A.D. supervised the project. A.C.Q. and C.G. wrote the manuscript, with input from all authors. A.D. was responsible for overall project direction, planning, and management.

Competing interests: The authors declare that they have no competing interests. **Data and materials availability:** All data needed to evaluate the conclusions in the paper are present in the paper and/or the Supplementary Materials.

Submitted 22 September 2021
Accepted 20 April 2022
Published 8 June 2022
10.1126/sciadv.abm5180